Chapter 6

Pulse Characterisation Techniques

A detailed investigation of complex molecular systems interacting with femtosecond laser radiation is only meaningful if one possesses all information about the laser pulses used in the experiment. Measurements of the beam energy, spectral distribution, spatial profile, and wave front can be easily done even in the case extremely short laser pulses. But the measurement of both, amplitude and phase, of very short laser pulses in the time domain is not a trivial problem.

First, methods for temporal pulse characterisation are described in this chapter. After that, spatial characterisation techniques of laser beams are presented. And finally, the energetic properties of laser pulses are described.

6.1 Temporal Pulse Characterisation

6.1.1 Methods of Temporal Pulse Characterisation

Usually, a short event can be characterised by another, even shorter event. Classical electronic techniques using fast streak cameras for temporal pulse width characterisation have, at best, a resolution of $\sim 0.5\,\mathrm{ps}$ [Kim03]. Hence, femtosecond pulse characterisation in the time domain requires other methods. These are based either on spectral interferometry or optical correlation techniques that make use of the short pulse itself. The simplest method is an "autocorrelation measurement". It provides minimum information namely the pulse duration[SGR87, TDF97]. There is some information on the pulse shape as well albeit symmetrised. The second method is the "frequency-resolved optical gating" (FROG) technique.

FROG involves a relatively simple experimental setup for determining the spectrally resolved autocorrelation function. Coupled with a mathematical algorithm this allows one to retrieve both the pulse amplitude and phase [Ktr93, DFT96, TDF97]. If a well characterised reference pulse is available, one may employ the so-called "cross-correlation frequency resolved optical gating" (XFROG). It involves measuring the spectrally resolved cross-correlation (sum frequency generation) of the unknown pulse with a full characterised reference pulse [LGK98, YFK01, DGX02]. Another method, based on spectral interferometry, is "spectral phase interferometry for direct electric-field reconstruction" (SPIDER) [IWa99, Dor99]. SPIDER is ideally suited for the characterisation of ultrashort single pulses [GSM99]. It combines a rather simple experimental setup with a robust and non-iterative mathematical algorithm for fast and noise insensitive pulse reconstruction. Moreover, the reconstructed pulse is free from ambiguities of time direction even when the second order nonlinearity is used. Combination of FROG and spectral interferometry leads to a new method which is known as "temporal analysis, by dispersing a pair of light electric fields" (TADPOLE). This technique does not use a nonlinear optical medium and therefore has an extremely high sensitivity [LCJ95, FBS96, DBL00]. But it requires that the spectral width of the unknown pulse is completely covered by the spectral width of the reference pulse.

Alternatively, different methods for temporal pulse characterisation can be applied. The preference of one or another method depends on a wide range of circumstances such as required accuracy of measurements, complexity of pulse structure, pulse duration, available pulse energy, or accessibility of a fully characterised reference pulse. In our case intensity autocorrelation and FROG technique are used for characterisation of the pulses directly delivered by the the laser system. The alignment of the shaper needs the possibility to control both amplitude and phase on-line. That is the reason why a SPIDER is employed for the shaper alignment. The same technique is used for the characterisation of sub-10 fs pulses. And finally, in pulse shaper experiments, where a reference pulse is available, the resulting complicated pulses are characterised by the XFROG method. A detailed description of all these techniques is given below.

6.1.2 Autocorrelation Measurement

Fig. 6.1 shows the setup for the intensity autocorrelation measurement used in the present

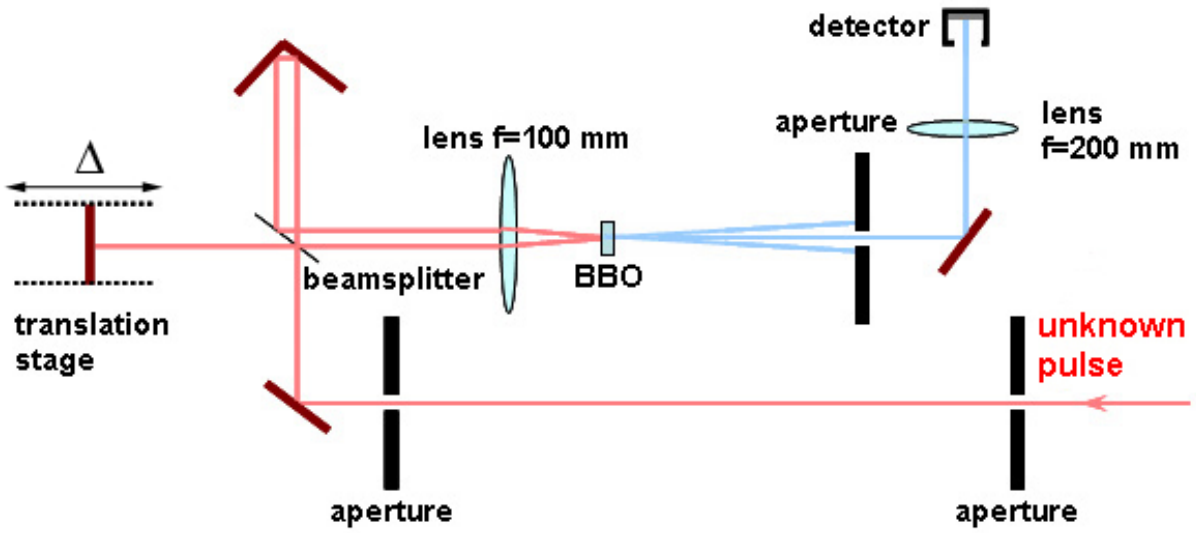

Figure 6.1: Schematic diagram of an autocorrelator (if the detector is a photodiode) or of a FROG setup (if the detector is a spectrometer).

work. The setup is designed to minimise temporal and spectral aberrations. The unknown pulse is split into two parts by a $50\% : 50\%$ thin (thickness of 1 mm) beamsplitter. One pulse is variably delayed with respect to the other pulse by passing through a computer controlled motorised translation stage. Then these pulses are focused by a lens with a focal length of 50 mm and overlapped under a crossing angle into a nonlinear optical medium, as a second harmonic generating (SHG) crystal. In the actual setup the type I of a beta-barium borate (BBO) crystal with a thickness of $50\,\mu$m is used. Such crystal thickness is small enough to minimise temporal smearing and to fulfil the conditions of phase matching [Wei83, OKG00]. It is important to mention that the crossing angle must be as small as possible to avoid losses of temporal resolution [TKS96, BPW99].

The SHG crystal produces a signal at twice the frequency of the input pulse in the direction of the bisector of the two incoming pulses. The autocorrelation signal is related to the intensities of the two incoming pulses by Eq. (5.17). An aperture lets pass only the autocorrelation signal. One extra reflection is used to remove the remaining radiation at the frequency of the input pulse. A 100 mm focal length lens focuses the autocorrelation signal onto a photodiode interfaced to a LabVIEW computer. To achieve better statistics the measurement of the autocorrelation signal (Eq. (5.17)) at each time delay δ is done for 1000 laser shots and a complete cycle of measurements is usually repeated at least 10 times. The minimal step of the

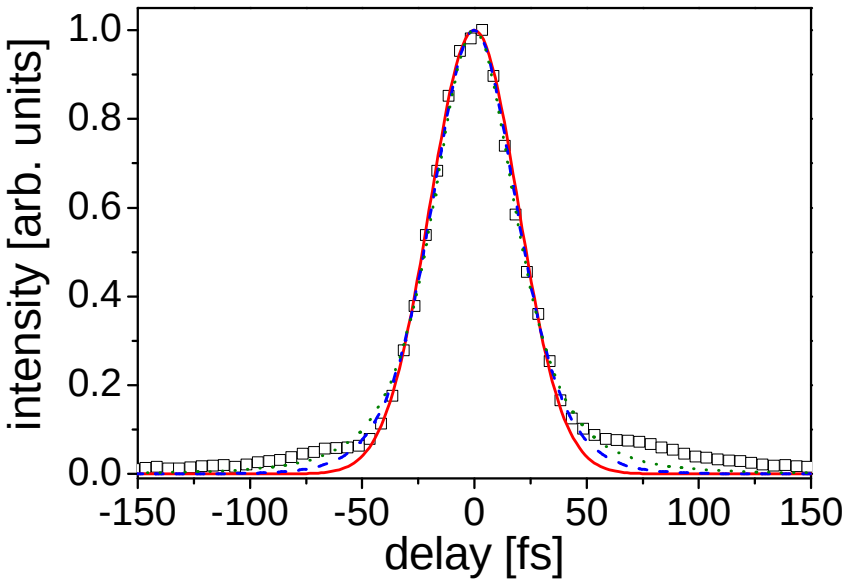

Figure 6.2: Pulse duration measurement by the autocorrelation technique for the pulse produced by the Multipass laser system. The measured autocorrelation is depicted by black open squares and fitted with Gaussian, sech^2, and Lorentzian functions as it is shown by full red, dashed blue, and dotted olive lines, respectively. The pulse durations (FWHM) are $32.77 \pm 0.46\,fs$, $29.09 \pm 0.34\,fs$, and $21.89 \pm 0.22\,fs$ according to Gaussian, sech^2, and Lorentzian fits, respectively.

time delay available from the motorised translation stage is 4 fs. The intensity autocorrelation shows a maximum at $\delta = 0$ and is always symmetrical. Autocorrelation measurements provide only a limited amount of information about an unknown pulse. Specifically, it contains no information about the phase of the pulse and the symmetry of any autocorrelation trace is a serious disadvantage for pulse form determination. To obtain information about the pulse width one has to make an intelligent guess about pulse shape. Generally, the full width at half-maximum (FWHM) of the unknown pulse τ is proportional to the FWHM of the measured intensity autocorrelation function τ_{AC}. But the proportionality factor (or deconvolution factor) varies significantly for different pulse shapes (see Sec. 5.1 and Eq. (5.18)).

Fig. 6.2 shows the autocorrelation measurement of the pulse produced by the Multipass laser system. The measured autocorrelation is depicted by black open squares and fitted

with Gaussian, sech^2, and Lorentzian functions as it is shown by full red, dashed blue, and dotted olive lines, respectively. The pulse durations (FWHM) obtained by Gaussian, sech^2, and Lorentzian fits are 32.77 ± 0.46 fs, 29.09 ± 0.34 fs, and 21.89 ± 0.22 fs, respectively. It is clear that the laser pulse duration determined in a such type of measurements strongly depends on the assumption about the pulse shape. Among these three fit functions the sech^2 one describes the measured data better excepting the region of rather large wings coming from a small pre-pulse which is not resolved in this measurement. Therefore, the sech^2 pulse shape is always assumed later on for the pulse duration estimations in autocorrelation measurements.

Also it is difficult to determine the presence or absence of some systematic or random errors in the measured autocorrelation function. Nevertheless, the autocorrelation measurement can be a powerful tool for the pulse width determination of simple pulses with an a priori known shape.

6.1.3 FROG Technique

As described above, the intensity autocorrelation measurements do not give sufficient information for full temporal characterisation of arbitrary shaped pulses. The FROG technique is free from the drawbacks of an autocorrelation measurement. This technique operating in the "time-frequency domain" involves both temporal resolution and frequency resolution simultaneously. FROG does this by spectrally resolving the signal pulse in any type of autocorrelation measurement performed in an instantaneously responding nonlinear medium. Depending on the nonlinear optical effect used for the signal pulse generation there are several FROG geometries such as polarisation gating (PG), self diffraction (SD), transient grating (TG), third harmonic generation (THG), and second harmonic generation (SHG) [TDF97].

SHG FROG was chosen in this work as a standard measurement technique for the characterisation of the pulses produced by the laser system because it is the most sensitive and simple FROG geometry. It involves only a second order nonlinearity. The main disadvantage of SHG FROG is the symmetry with respect to the time delay and, hence, SHG FROG has an ambiguity in the direction of time. This ambiguity can be removed in one of several ways [TDF97]. Practical implementation of this technique is done using the setup shown in Fig. 6.1, where the SHG signal is spectrally resolved by the spectrometer (AvaSpec-2048, Avantes BV). The spectral resolution of the spectrometer is 0.17 nm and it is enough for these purposes.

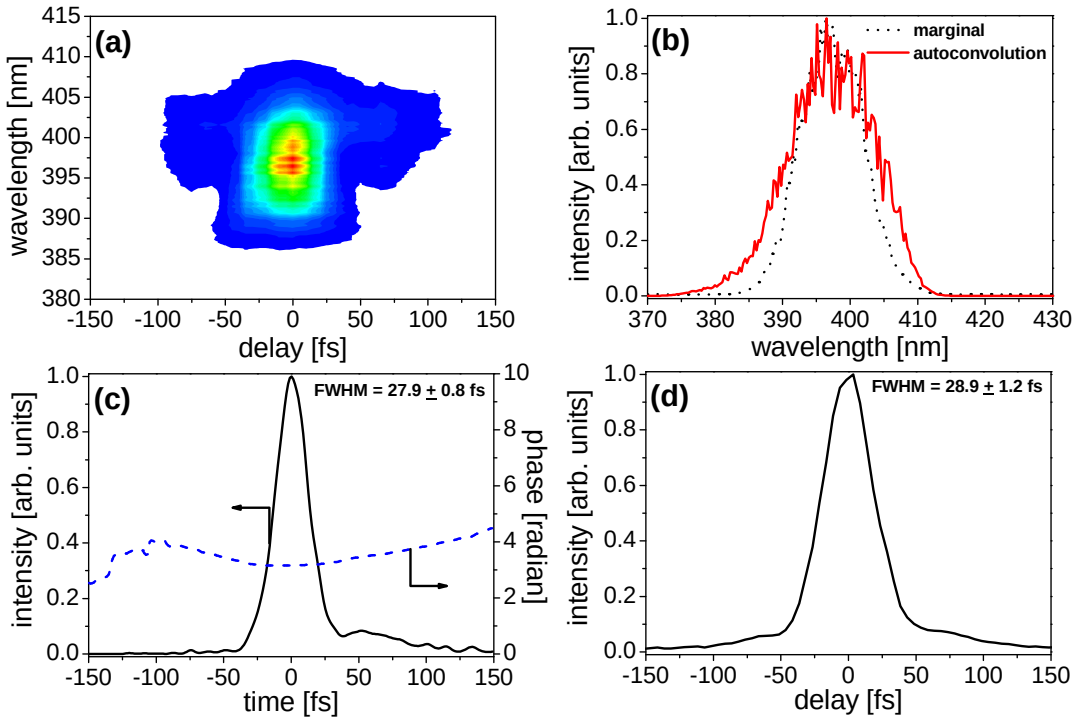

Figure 6.3: Temporal characterisation of the pulses produced by the Multipass laser system: (a) recorded FROG map; (b) frequency marginal and autoconvolution; (c) reconstructed temporal intensity and phase from the FROG map; (d) measured autocorrelation function.

The spectral response of the spectrometer is calibrated using a source of well-characterised emission spectrum.

The spectrogram of the signal pulse in SHG FROG is given by

$$I_{FROG}^{SHG}(\omega,\delta) = \left| \int_{-\infty}^{\infty} E(t)E(t-\delta)e^{-i\omega t}\,dt \right|^2 \quad . \tag{6.1}$$

In contrast to the autocorrelation measurements described by Eq. (5.17) this spectrogram provides an unknown pulse representation as a two dimensional function of frequency and delay time and comprises essential information required for full pulse characterisation. One example of a spectrogram or "SHG FROG map" is shown in Fig. 6.3a. This is the spectrogram of the pulses produced by the Multipass laser system. Any FROG map is a type of time-frequency distribution that contains all relevant information about the pulse. An iterative pulse retrieval algorithm extracts the pulse intensity and phase from a FROG map by finding the electric

field that best reproduces the map. It must be mentioned before discussing the algorithm that FROG provides consistency checks not available with autocorrelation measurements. An electric field sampled at N points has $2N$ degrees of freedom (N points of both magnitude and phase), but it corresponds to a FROG map with N^2 points. The fact that the FROG map contains redundant data allows for such checks. This is accomplished by comparing the "frequency marginal" of the FROG map with the independently measured pulse spectrum [DFT96, TDF97]. The frequency marginal is the FROG map integrated with respect to the delay

$$M^f_{FROG}(\omega) = \int_{-\infty}^{\infty} I^{SHG}_{FROG}(\omega, \delta)\, d\delta \quad . \tag{6.2}$$

The frequency marginal has to be equal to the autoconvolution of the fundamental pulse spectrum $S(\omega)$

$$M^f_{FROG}(\omega) = \int_{0}^{\infty} S(\omega' - 2\omega_0) S(\omega' - \omega) d\omega' \quad , \tag{6.3}$$

where ω_0 is the carrier frequency. A systematic experimental error such as incorrect wavelength or temporal calibrations of FROG data, insufficient doubling crystal bandwidth, spatial or temporal distortions of the pulses at the focus can be a reason of non-agreement of the SHG FROG frequency marginal with the autoconvolution of the pulse spectrum. Fig. 6.3b shows an example of how the frequency marginal can be used to check the validity of SHG FROG measurements. There is rather good agreement of the frequency marginal with the autoconvolution of the measured spectrum. Small narrowing of the frequency marginal is explained by insufficient doubling crystal bandwidth or/and other bandwidth losses in the FROG setup. Thus, this marginal provides a powerful check of the experimental apparatus. Moreover, it is possible to correct the measured FROG map by multiplying its with a ratio of the fundamental pulse spectrum autoconvolution and the frequency marginal. There is also a "delay marginal"

$$M^d_{FROG}(\delta) = \int_{0}^{\infty} I^{SHG}_{FROG}(\omega, \delta)\, d\omega \quad , \tag{6.4}$$

which is essentially the same as an autocorrelation function and can be used for a quick estimation of τ.

As already mentioned, the information contained in the FROG map is sufficient for a full determination of amplitude and phase of the pulsed electric field. The goal of pulse retrieval algorithm is to find an $E(t)$ that satisfies Eq. (6.1). Several modification of FROG pulse retrieval algorithms were developed and can now be used for electric field reconstruction.

The simplest of them, but a very powerful one, is the method of generalised projections [DFT94, TDF97]. This algorithm starts the first iteration with an initial guess of the pulsed field $E(t)$ and reconstructs the FROG map using Eq. (6.1). Then the FROG error G is calculated as an rms difference between the measured FROG map $I_{FROG}(\omega_i, \delta_j)$ and the reconstructed FROG map $I^{(k)}_{FROG}(\omega_i, \delta_j)$

$$G = \sqrt{\frac{1}{N^2}\sum_{i,j=1}^{N}\left|I_{FROG}(\omega_i,\delta_j) - \alpha I^{(k)}_{FROG}(\omega_i,\delta_j)\right|^2} \quad , \tag{6.5}$$

where N is a size of the FROG map array, α is the real number for the renormalisation, and k is the number of the iteration step. The algorithm analyses the FROG error G and generates a new guess for $E(t)$ using the method of generalised projections. Then the initial guess is replaced with a new one and the whole procedure is repeated in a cycle. The goal of the algorithm is to find such a pulsed field $E(t)$ that minimises the FROG error G. For our purposes of pulse characterisation the commercial program (FROG 3.0.9, Femtosoft Technologies) is used. This program allows one to use several retrieval algorithms. The measured FROG map together with the retrieved amplitude and phase of the pulses delivered by the laser system is shown in Fig. 6.3a and Fig. 6.3c, respectively.

6.1.4 XFROG Method

For the temporal characterisation of *shaped pulses with complicated structure* XFROG is applied. In this technique a fully characterised reference pulse is overlapped with the unknown pulse to be characterised in the BBO crystal. The spectrally resolved sum frequency signal is measured as a function of the delay between the reference and the unknown pulse and gives the XFROG map

$$I^{SHG}_{XFROG}(\omega,\delta) = \left|\int_{-\infty}^{\infty} E_{unknown}(t)E_{ref}(t-\delta)e^{-i\omega t}\,dt\right|^2 \quad . \tag{6.6}$$

Both XFROG and SHG FROG use the same nonlinear process. But the SHG FROG involves only one replica of an unknown pulse, while the XFROG involves two pulses that are not identical. This leads to additional advantages of the XFROG technique. The main one is the absence of a time ambiguity in XFROG maps. XFROG maps are more accessible to intuition than FROG maps. Also this technique is better suited for characterisation of weak pulses. The XFROG setup is similar to the FROG setup as shown in Fig. 6.4. A thin glass plate with a

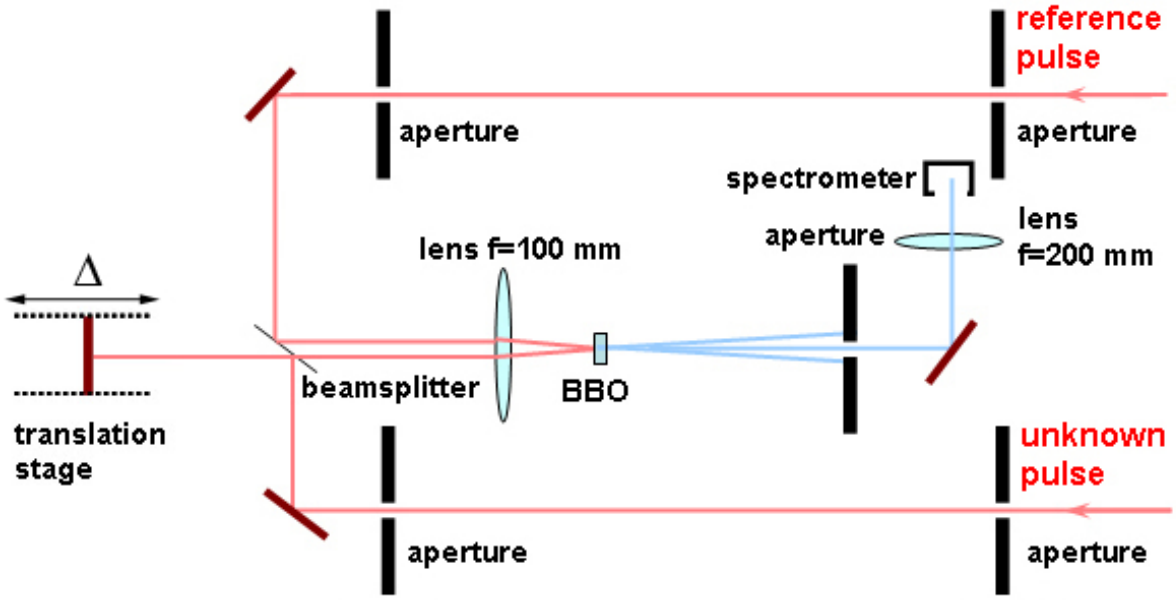

Figure 6.4: Schematic diagram of a cross-correlator (if the detector is a photodiode array) or of an XFROG setup (if the detector is a spectrometer).

reflectivity of only $0.4\,\%$ is inserted into the laser beam path just in front of the shaper to create the reference pulse. Phase and amplitude distribution of this pulse are determined by a FROG as discussed above, and then used as the fully characterised reference. An additional delay line is introduced to equalise the optical paths of both pulses, the reference pulse and the pulse emerging from the the shaper which is to be characterised. The reference pulse is overlapped with the unknown pulse in a BBO crystal. The sum frequency signal is measured for different delays between the reference and the unknown pulse, thus generating the XFROG map. This XFROG map then is used to reconstruct phase and amplitude of the unknown pulse, using commercial XFROG software (FROG 3.0.9, Femtosoft Technology). Fig. 6.5a and Fig. 6.5c show an XFROG map and the reconstructed amplitude and phase for the pulse propagated though the shaper without applying any extra phase on it. Some pulse lengthening and pulse shape distortions for the pulse propagated though the shaper as compared to the incoming one are caused by the bandwidth losses in the shaper setup and unavoidable optical aberrations induced in the shaper.

6.1.5 SPIDER Technique

During the shaper alignment a temporal pulse characterisation is performed using the

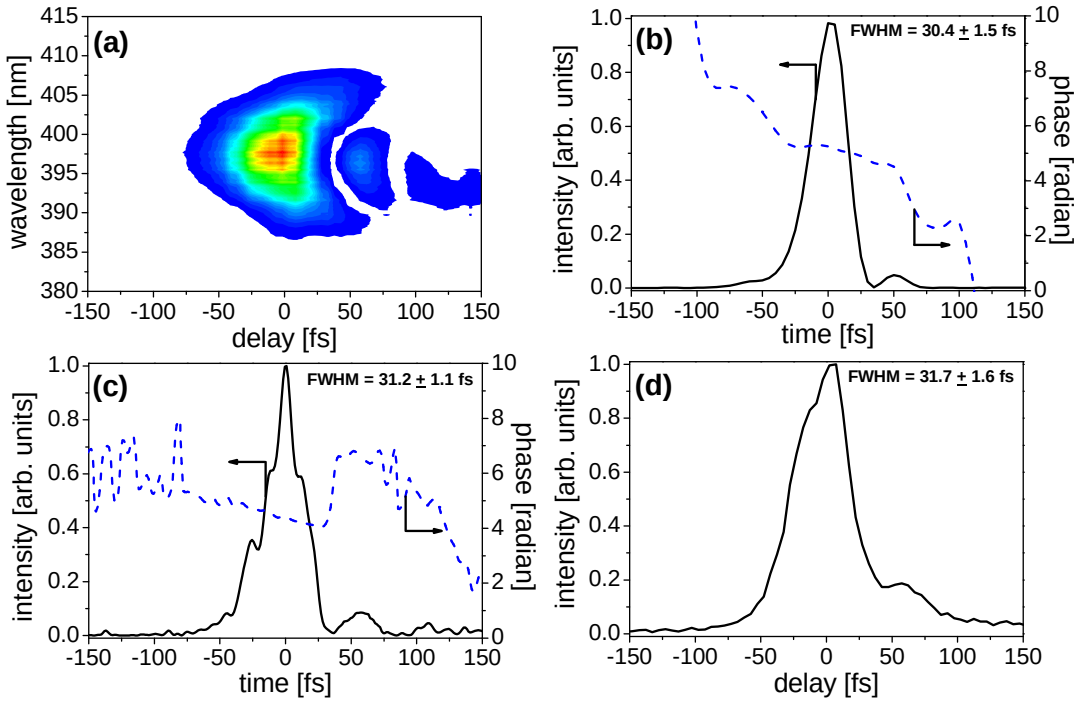

Figure 6.5: Temporal characterisation of the pulses passed through the shaper setup: (a) measured XFROG map; (b) temporal intensity and phase measured with SPIDER technique; (c) reconstructed temporal intensity and phase from an XFROG map; (d) measured cross-correlation.

SPIDER technique (APE Spider, APE GmbH). The same technique is also employed for the temporal characterisation of the sub-10 fs pulses. This interferometric technique is based on nonlinear conversion of two temporally delayed replicas of an unknown pulse with a stretched pulse[GSM99, SWW99].

The principle of a SPIDER is shown in Fig. 6.6a. An unknown pulse is split into two replicas with a constant time delay δ between each another using a glass etalon or Michelson interferometer. These replicas are with a stretched, chirped pulse in a nonlinear medium. The chirped pulse is produced by stretching a part of the unknown pulse itself (alternatively, one may use a pulse from an external source) in a dispersive delay line. This can be a block of dispersive material (glass) as well as a pair of prisms or gratings. The width of the chirped pulse has to be much larger than the time delay δ. Since there is a time delay between the replicas, each pulse replica is upconverted in the nonlinear medium with a different frequency

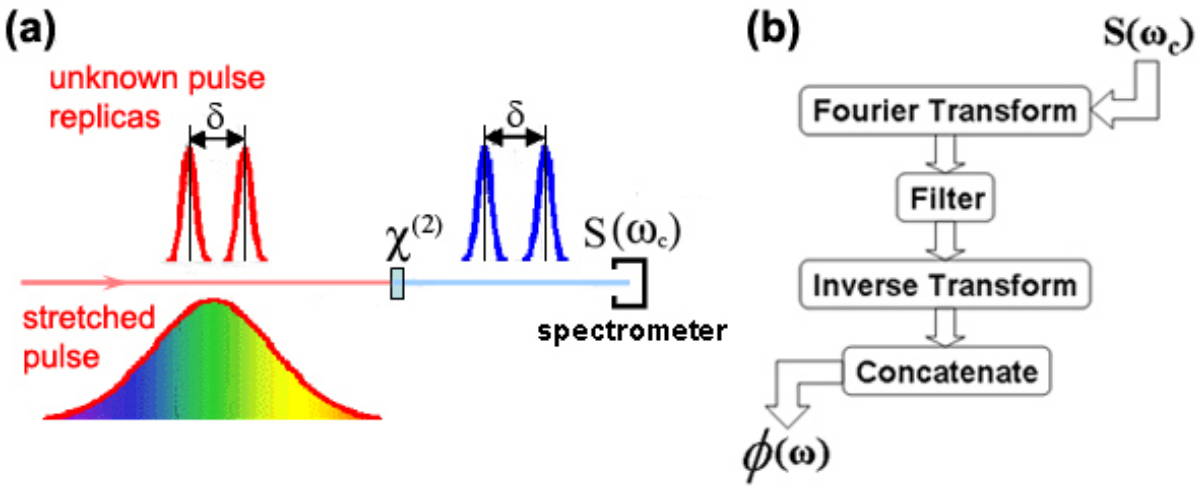

Figure 6.6: Principle of SPIDER apparatus: (a) SPADER optical layout; (b) algorithm for the spectral phase reconstruction [IWa98]. For details see text.

slice of the chirped pulse, and consequently, the two upconverted pulses have slightly different frequencies. The result of the mixing is two temporally delayed and spectrally shifted replicas which interfere in a spectrometer producing an interferogram

$$S(\omega_c) = |E(\omega_c)|^2 + |E(\omega_c+\Omega)|^2 + 2\,|E(\omega_c)E(\omega_c+\Omega)| \times \\ \times \cos\left[\phi(\omega_c+\Omega) - \phi(\omega_c) + \omega_c\delta\right] \quad , \tag{6.7}$$

where ω_c is the central frequency of the pulse, δ is the fixed delay time between replicas, Ω is the the frequency shift or the amount of spectral shear, $E(\omega_c)$ is the pulse electric field in frequency domain, $\phi(\omega_c)$ is the pulse phase. From this spectrogram it is possible to calculate the spectral phase of the unknown pulse. For exact phase reconstruction the spectral shear must satisfy the Whittaker-Shannon sampling theorem [Goo96]. The value of the spectral shear is adjusted by changing the second order dispersion of the stretched pulse. In addition, the interferogram sampling interval has to be not greater than the Nyquist limit [Goo96]. With the calculated spectral phase, an additional measurement of the unknown pulse spectrum allows one to completely characterise such pulse.

A robust non-iterative mathematical procedure can be used for the spectral phase extraction from the measured spectral interferogram [TIK82]. This procedure is schematically shown in Fig. 6.6b. First, the interferogram is Fourier transformed into the time domain. The result of this transformation gives three peaks centred at $t = 0, \pm\delta$. The peak near zero time ($t = 0$) is due to the constant terms in Eq. (6.7), while the peaks at $t = \pm\delta$ are due to the cosine

term. Each of these two peaks possesses all phase information. The peaks at $t = -\delta, 0$ are removed by filtering and the remaining peak at $t = \delta$ is inverse Fourier transformed back to the frequency domain. After subtraction of the linear term $\omega\delta$ that is due to the delay δ, the remaining part is the phase difference between two frequencies separated by the spectral shear Ω: $\phi(\omega_c + \Omega) - \phi(\omega_c)$. Finally, the spectral phase of the unknown pulse for a discrete set of frequencies is reconstructed by concatenation of the phase in steps of Ω.

A result of the SPIDER technique applied to characterise a pulse propagated through the shaper is shown in Fig. 6.5b. This result is rather similar to the one obtained with the XFROG technique (Fig. 6.5c). Mainly, the difference between these two results comes from a fact that these measurements were done in two different days. Larger distortions of the pulse structure in the case of the XFROG technique are due to the iterative nature of the pulse reconstructive algorithm. Nevertheless, both techniques found characteristic features of the temporal pulse structure and determined essentially the same τ. Therefore, both SPIDER and XFROG techniques can be employed for the temporal characterisation of femtosecond laser pulse.

6.2 Spatial Laser Beam Characterisation

An idealised Gaussian beam can be considered as good approximation for the simplest types of beams provided by laser sources. Its spatial parameters and propagation properties are well known [BWo99]. But real beams deviate more or less from this idealised description. The closest physical approach to the idealised Gaussian beam is the rotationally symmetric beam from a low power TEM_{00} laser. For the sake of simplicity, only such type of beams is analysed below.

Spatial characterisation of a laser beam at the focal point is very important for the determination of the interaction volume, laser fluence, and intensity. The essential information lies in the knowledge of the spot size of a focused laser beam. Usually in laser physics the spot size is depicted by w (a radius at which the intensity drops down to $1/e^2$ with respect to its maximum value).

There are many techniques of measuring laser beam sizes [AHM71, SWe81, KLa83, HKo91]. If the radius of the focal spot is larger than the laser wavelength ($w \gg \lambda$), the intensity profile

can be imaged by a CCD camera [MMR01] or simply be recorded by measuring the intensity passed by a knife-edge scanning the laser beam in the focal plane [AHM71, FHS77]. Smaller spots can be characterised using different modifications of the knife-edge scan technique [STa75, CLL84, CGC86] or Ronchi ruling method [CLL84, CGC86].

Under the action of a focusing mirror (lens) with a focal length f and assuming a parallel monochromatic Gaussian input beam, one can calculate the beam waist at the focal plane w_f with the following formula

$$w_f = \frac{f\lambda}{\pi w_0} \quad , \tag{6.8}$$

where w_0 is the waist of the unfocused beam. Both waists have to be measured at $1/e^2$ level. The measurement of the unfocused laser beam waist w_0 is much simpler than the measurement of w_f at the focal plane. Therefore, one can measure the waist of the unfocused laser beam and estimate the beam waist at the focal plane using Eq. (6.8). However, Eq. (6.8) assumes the perfect focussing conditions which can not be always satisfied for real laser systems. Hence, the direct measurement of the beam waist at the focal plane is more accurate and desirable.

In the present studies such measurement is done using the knife-edge scan at the focal plane of the focusing mirror [FHS77], where a thin metallic plate is translated across the laser beam and the intensity is recorded as a function of the plate position. For this measurement the pulse energy has to be diminished by the several reflections from uncoated glass for the reduction of the pulse intensity at the focal plane below the damage threshold of the metallic plate used for the scanning. The spatial intensity distribution $I(x, y)$ of a Gaussian beam at the focal plane is

$$I(x, y) = \frac{2P_0}{\pi w^2} e^{-2\frac{x^2+y^2}{w^2}} \quad , \tag{6.9}$$

where P_0 is the total laser power, x and y are coordinates in the plane perpendicular to the beam axis. The origin of this coordinate system is taken on the beam axis. If the beam is partly blocked by a plate aligned parallel to the y axis, the transmitted laser power is

$$\begin{aligned} P(x_0) = \int_{-\infty}^{\infty}\int_{x_0}^{\infty} \frac{2P_0}{\pi w^2} e^{-2\frac{x^2+y^2}{w^2}}\, dydx = \frac{\sqrt{2}}{\sqrt{\pi}} P_0 \int_{x_0}^{\infty} \frac{1}{w} e^{-\frac{2x^2}{w^2}}\, dx = \\ = \frac{1}{2} P_0 \operatorname{erfc}\left(\frac{\sqrt{2}}{w} x_0\right) \quad , \end{aligned} \tag{6.10}$$

where x_0 is the current position of the plate edge on the x axis. By scanning the x coordinate with the plate and recording the transmitted laser power $P(x)$ as a function of x, the beam

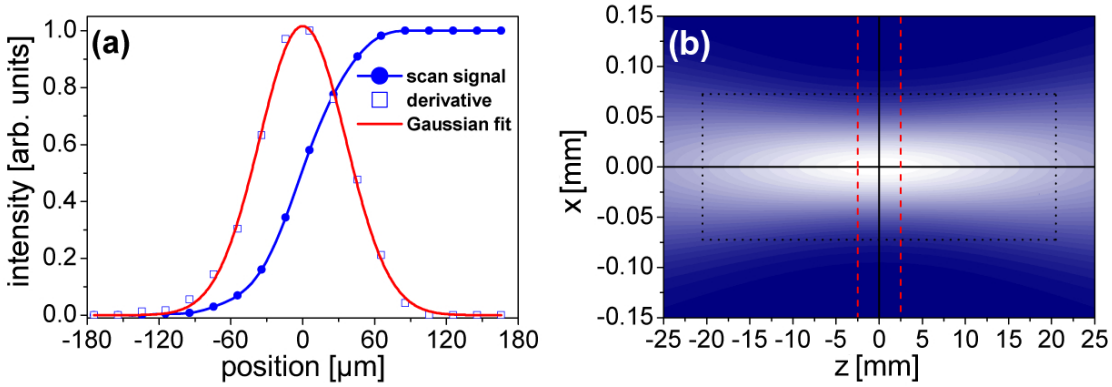

Figure 6.7: Spatial beam characterisation: (a) measured knife-edge scan of the laser beam for the Multipass laser system, its derivative, and Gaussian fit; (b) calculated spatial intensity distribution using the waist obtained in Fig. 6.7a. The laser propagates in z direction. The horizontal black dotted lines shows the beam waist w. The vertical black dotted lines give the Rayleigh region. The red dashed lines indicate the molecular beam interacting with the laser beam.

profile along the x axis is obtained by the differentiation of the recorded signal. To get the beam profile in the perpendicular direction one has to repeat this procedure for the scanning along y axis. Fig. 6.7a illustrates the result of a typical scan at the focal plane of a concave mirror with $f = 50\,\text{cm}$ for the Multipass laser system. The derivative of this scan is fitted by a Gaussian function with $w = 72.3 \pm 1.1\,\mu\text{m}$.

Close to the focal plane the beam collimation along the direction of propagation is characterised by the Rayleigh length z_R

$$z_R = \frac{\pi w^2}{\lambda} \quad , \tag{6.11}$$

defined as the distance between the focal plane and the plane at which the beam waist increases by a factor of $\sqrt{2}$. For the waist measured in Fig. 6.7a $w = 72.3\,\mu\text{m}$, the corresponding Rayleigh length is $z_R = 20.5\,\text{mm}$. The distance between the points $\pm z_R$ about the waist is called the confocal parameter

$$b = 2z_R \tag{6.12}$$

of the beam. Fig. 6.7b shows a (calculated) map of the spatial intensity distribution around the focal plane for a focused laser beam centred at the wavelength of $800\,\text{nm}$. The beam propagates along the z axis and has radial symmetry with respect to this axis at $x, y = 0$.

The focal plane is perpendicular to both the picture plane and z axis. It is located at $z = 0$. The beam symmetry axis and the focal plane are indicated by solid lines. The beam waist $w = 72.3\,\mu$m and the confocal parameter $b = 41$ mm are shown by the black dotted lines. As discussed in Sec. 4.2, the diameter of the effusive molecular beam used in this work is only $D_M = 5$ mm at the point, where the molecular beam crosses the laser beam. The red dashed lines in Fig. 6.7b represent the molecular beam. Since the Rayleigh length is larger than the molecular beam diameter it is straightforward to assume for the experimental geometry used in the present work that the interaction region is a cylinder with the radius w and the length D_m. Intensity variations along the cylinder axis in this case are negligible small.

6.3 Pulse Intensity and Fluence

Intensity and fluence are two most important attributes of laser radiation when describing laser-matter interaction. Mainly, intensity is considered in the present work for this characterisation.

The intensity $I(r,t)$ of an ideal Gaussian laser pulse at a given time t and a distance r from the beam axis can be written as

$$I(r,t) = I_0 e^{-2\left(\frac{r}{w}\right)^2} e^{-4\ln 2\left(\frac{t}{\tau}\right)^2} \quad , \tag{6.13}$$

where I_0 is the pulse peak intensity, τ is a temporal FWHM, and w is a beam waist (a radius at which the intensity drop down to $1/e^2$ with respect to its maximum value). Sometimes, the beam radius is measured at levels, where the intensity decreases to $1/e$ ($w_{1/e}$) or $1/2$ ($w_{1/2}$). These two quantities relate to w as

$$w_{1/e} = \frac{\sqrt{2}}{2} w \tag{6.14}$$

and

$$w_{1/2} = \sqrt{\frac{\ln 2}{2}} w \quad . \tag{6.15}$$

Both spatial and temporal integration of Eq. (6.13) leads according to [HSc09] (see Eq. (13.67)) to the pulse energy

$$W = I_0 \int_0^\infty e^{-2\left(\frac{r}{w}\right)^2} \int_{-\infty}^\infty e^{-4\ln 2\left(\frac{t}{\tau}\right)^2} dr dt = I_0 \frac{\pi\sqrt{\pi}}{4\sqrt{\ln 2}} w^2 \tau \quad . \tag{6.16}$$

The pulse energy can be quite easy measured by a photodetector. In this work, it is done using the pyroelectric laser energy metre (TPM-300CE, Gentec Electro-Optics, Inc.). The peak intensity is obtained from Eq. (6.16) by term rearrangement

$$I_0 = \frac{4\sqrt{\ln 2}}{\pi\sqrt{\pi}}\frac{W}{w^2\tau} = \frac{2\sqrt{\ln 2}}{\pi\sqrt{\pi}}\frac{W}{w_{1/e}^2\tau} = \frac{2\sqrt{\ln^3 2}}{\pi\sqrt{\pi}}\frac{W}{w_{1/2}^2\tau} \quad . \tag{6.17}$$

Intensity is commonly measured in units of [W/cm^2]. Only spatial integration of Eq. (6.13) gives the time dependent pulse power (the amount of energy per unit of time)

$$P(t) = I_0 e^{-4\ln 2\left(\frac{t}{\tau}\right)^2}\int_0^\infty e^{-2\left(\frac{r}{w}\right)^2} dr = I_0\frac{\pi}{2}w^2 e^{-4\ln 2\left(\frac{t}{\tau}\right)^2} \quad . \tag{6.18}$$

The peak power P_0 is obtained from Eq. (6.18) at $t = 0$

$$P_0 = P(0) = I_0\frac{\pi}{2}w^2 = I_0\pi w_{1/e}^2 = I_0\frac{\pi}{\ln 2}w_{1/2}^2 \quad . \tag{6.19}$$

The peak intensity is simply equal to the pulse peak power divided by the waist area measured at $1/e$ level as mentioned in [HSc09].

Integration of Eq. (6.13) over time only gives the fluence (the amount of energy per unit of area)

$$F(r) = I_0 e^{-2\left(\frac{r}{w}\right)^2}\int_{-\infty}^\infty e^{-4\ln 2\left(\frac{t}{\tau}\right)^2} dt = I_0\frac{\sqrt{\pi}}{2\sqrt{\ln 2}}\tau e^{-2\left(\frac{r}{w}\right)^2} \quad . \tag{6.20}$$

The fluence is usually measured in units of [J/cm^2]. The peak fluence F_0 is obtained from Eq. (6.20) at $r = 0$

$$F_0 = F(0) = I_0\frac{\sqrt{\pi}}{2\sqrt{\ln 2}}\tau \quad . \tag{6.21}$$

Using Eq. (6.16) the expressions for peak power and peak fluence can be rewritten as

$$P_0 = \frac{2\sqrt{\ln 2}}{\sqrt{\pi}}\frac{W}{\tau} \tag{6.22}$$

and

$$F_0 = \frac{2}{\pi}\frac{W}{w^2} \quad . \tag{6.23}$$

Since the pulse energy, the pulse duration (Sec. 6.1), and the beam waist (Sec. 6.2) are measurable, the intensity, the power, and the fluence can be calculated using Eq. (6.17), Eq. (6.22), and Eq. (6.23), respectively.